

The Impact of Ligand Removal on the Optoelectronic Properties of Inorganic and Hybrid Lead Halide Perovskite Nanocrystal Films

Paris Papagiorgis,* Marios Sergides, Andreas Manoli, Modestos Athanasiou, Caterina Bernasconi, Fedros Galatopoulos, Apostolos Ioakeimidis, Constantinos Nicolaidis, Epameinondas Leontidis, Theodossis Trypinotis, Stelios Choulis, Maryna I. Bodnarchuk, Maksym V. Kovalenko, Andreas Othonos, and Grigorios Itkos*

Ligand exchange performed during or after the colloidal synthesis of nanocrystals (NCs) provides an efficient way to produce conductive NC solids for optoelectronics. Herein, a post-synthetic ligand washing process is developed and applied to two different combinations of ligands and perovskite NCs, namely robust green CsPbBr₃ NCs capped by didodecyldimethylammonium bromide and near-infrared FAPbI₃ NCs decorated by weakly bound oleic acid ligands. The impact of such processes on the morphological and optoelectronic NC properties is examined while exploring parameters such as the reaction time and the influence of oxygen and humidity. For the FAPbI₃ NCs, ligand washing results in extended NC aggregation and substantial photoluminescence loss, with the treatment becoming more aggressive for air-exposed films. For the CsPbBr₃ NCs, the process is insensitive to the environmental conditions and results in partial ligand shell loss and NC close packing rather than bulk-like aggregation while affecting less the optical properties. Upon ligand removal, the photoconductance increases by up to $\approx 90\%$ and $\approx 60\%$ for FAPbI₃ NCs and CsPbBr₃ NCs, respectively. THz spectroscopy produces qualitatively similar trends of the conductivity with ligand removal time, with THz mobility values as high as 30 and 6 V⁻¹s⁻¹cm² for glove box prepared FAPbI₃ and CsPbBr₃ NCs, respectively.

1. Introduction

Lead halide perovskite nanocrystals (LHP NCs) have emerged as high-performance remote emitters for luminescent, lasing, and single photon applications, also finding niche uses in various other electro-optical devices such as photodetectors, sensors, and solar cells.^[1–3] The performance of such devices is crucially dependent on the preparation of conductive, close-packed LHP NC layers. Various successful electronic functionalization approaches have been implemented that include the use of short ligand complexes during the colloidal synthesis^[4–6] as well as post-synthetic ligand exchange^[7–9] or ligand removal methods.^[10–12] In the latter approach, the active layer is typically exposed to antisolvents such as methyl acetate (MeAc), or ethyl acetate (EtAc) followed by passivation treatment by cation halide salts.^[7,10–12] In such treatments, the bulky ligands that hinder conductivity are removed and the active layer is built up by casting multiple

P. Papagiorgis, A. Manoli, M. Athanasiou, G. Itkos
Department of Physics
Experimental Condensed Matter Physics Laboratory
University of Cyprus
Nicosia 1678, Cyprus
E-mail: papagiorgis.paris@ucy.ac.cy; itskos@ucy.ac.cy

M. Sergides, A. Othonos
Department of Physics
Laboratory of Ultrafast Science
University of Cyprus
Nicosia 1678, Cyprus

C. Bernasconi, M. I. Bodnarchuk, M. V. Kovalenko
Institute of Inorganic Chemistry
Department of Chemistry and Applied Biosciences
ETH Zürich
Zürich CH-8093, Switzerland

C. Bernasconi, M. I. Bodnarchuk, M. V. Kovalenko
Laboratory for Thin Films and Photovoltaics
EMPA—Swiss Federal Laboratories for Materials Science and Technology
Überlandstrasse 129, Dübendorf CH-8600, Switzerland

The ORCID identification number(s) for the author(s) of this article can be found under <https://doi.org/10.1002/adom.202301501>

© 2023 The Authors. Advanced Optical Materials published by Wiley-VCH GmbH. This is an open access article under the terms of the [Creative Commons Attribution](https://creativecommons.org/licenses/by/4.0/) License, which permits use, distribution and reproduction in any medium, provided the original work is properly cited.

DOI: 10.1002/adom.202301501

layers of the material while being exposed to the salts that heal the surface defects produced by the ligand desorption and preserve the three-dimensional perovskite phase. By employing such as method for the first time, Sanehira et al.^[10] demonstrated solar cells based on closed-packed arrays of CsPbI₃ NCs with power conversion efficiency (PCE) over 10%. The use of Formamidinium Iodide (FAI) post-treatment, improved the PCE to $\approx 14\%$ ^[13] while subsequent optimization involving the use of NC multinary compositions and heterojunctions^[8,14,15] allowed a further leap in the efficiency, reaching efficiencies of $\approx 17.4\%$.^[16–18]

Herein, we develop a ligand removal protocol aiming to fabricate thick and conductive LHP NC films for light harvesting applications. The versatility of the approach is being demonstrated by applying it into two substantially different combinations of ligands and NC materials, namely all-inorganic, green absorbing CsPbBr₃ NCs capped by robust didodecyldimethylammonium bromide-lead bromide (DDAB-PbBr₂) molecules and near-infrared hybrid FAPbI₃ NCs decorated by weakly bound oleic acid (OA) and oleylamine (OAm) ligands. The two types of NC-ligand materials have been selected based on their well-studied structural and photophysical properties and their chemical robustness when imposed to the ligand-washing treatment. A parametric series of samples has been fabricated in inert and ambient conditions and imposed to the respected ligand stripping process, i.e., CsPbBr₃ NCs were exposed to CsBr solution in EtAc and FAPbI₃ NCs exposed to FAI in EtAc. The structural properties of the samples were probed by scanning electron microscopy (SEM) and atomic force microscopy (AFM), monitoring the NC aggregation process as ligands were removed. Optical spectroscopy was implemented to study the impact of the progressively smaller ligand coverage on the NC exciton energetics and dynamics, while the electronic communication within the NC solids was probed via a combination of time-domain THz spectroscopy (TDS), time-resolved THz spectroscopy (TRTS) and photoconductive lateral NC devices.

2. Results and Discussion

The motivation of the work has been the adaptation of CsPbI₃ NC ligand removal methodologies for solar cells^[7,10–12] to the hybrid NC counterpart material of FAPbI₃. The latter, possesses a narrower energy gap, making it more suitable for solar light absorption and has been found to retain the perovskite black phase more efficiently compared to CsPbI₃.^[19,20] The aforementioned recipes

successfully produce high mobility CsPbI₃ NC arrays via layer-by-layer deposition involving ligand washing by a polar solvent formulation such as lead(II) nitrate in MeOAc^[7] and subsequent treatment by cation halide in EtAc to allow ligand desorption, defect passivation and ensure electronic coupling of the NCs. Application of this ligand removal protocol to FAPbI₃ NC films in both inert and ambient conditions was found to increase the film conductivity by order(s) of magnitude but also led to rapid degradation of the material, as washing by the MeOAc formulation was found to induce a black to yellow FAPbI₃ crystal phase transformation. The developed simplified version of the protocol, schematically shown in **Figure 1**, does not include the MeOAc washing step but instead uses a single process of ligand removal by EtAc and simultaneous FAI salt passivation that is repeated to build a layer-by-layer NC assembly followed by PMMA over-layer encapsulation. To test the applicability and versatility of the method, the treatment was also applied to all inorganic CsPbBr₃ NCs capped by didodecyldimethylammonium bromide and treated by lead bromide (DDAB-PbBr₂). The DDAB/PbBr₂ ligands provide highly efficient surface passivation and defect healing, making DDAB/PbBr₂-CsPbBr₃ NCs suitable for a plethora of light-emitting applications.^[21–26] In direct analogy to the FAPbI₃ NC system, CsPbBr₃ NCs were exposed to a single step of washing by a CsBr solution in EtAc. All work was performed on inorganic and hybrid NCs in the weak confinement regime with similar sizes in the range of 10–12 nm to minimize the impact of NC size on the produced results and trends. Representative optical properties and TEM images of dilute solutions of the pristine NCs are presented in **Figure S1** (Supporting Information).

The impact of the treatment reaction time (t_{reac}) was studied in the range of 0–20 s, with zero referring to untreated samples. Further exposure to 20 s to the washing formulation leads to crystal damage or phase transformations and deterioration of the optoelectronic properties of the materials. The effect of humidity and oxygen was also probed, as two identical series of films per NC material were fabricated and processed in the inert environment of the glove box and in ambient conditions with $\approx 40\%$ humidity. **Table 1** lists the series of the discussed samples with the corresponding reaction time.

2.1. Morphological and Optical Spectroscopy Study

2.1.1. FAPbI₃ NCs

The evolution of the film microstructure with t_{reac} was studied via SEM and AFM microscopy. SEM images of FA0 to FA20 samples, fabricated in inert glove box conditions, are displayed in **Figure 2a–h**. A relatively smooth morphology was observed in the pristine FA0 sample. As ligand washing reaction time increases, aggregation of NCs occurs, resulting in the growth of progressively larger FAPbI₃ domains. The high-resolution SEM images (**Figure 2e–h**) indicate that aggregation produces mainly irregular-shaped grains and some more regular-shaped FAPbI₃ crystallites, with the latter becoming more prominent for longer ligand washing times. Particle size SEM analysis is presented in **Figure 2i–n**, with output parameters displayed in **Table S1** (Supporting Information). The analysis indicates a bimodal Gaussian areal distribution of FAPbI₃ grains peaked at $\approx 400 \text{ nm}^2$ for all

F. Galatopoulos, A. Ioakeimidis, S. Choulis
Molecular Electronics and Photonics Research Unit
Department of Mechanical Engineering and Materials Science and Engineering
Cyprus University of Technology
Limassol 3036, Cyprus
C. Nicolaides, T. Trypiniotis
Department of Physics
University of Cyprus
Nicosia 1678, Cyprus
E. Leontidis
Department of Chemistry
University of Cyprus
Nicosia 1678, Cyprus

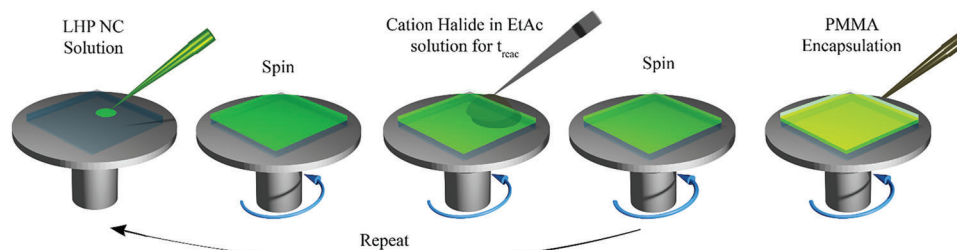


Figure 1. Schematic of the NC film treatment and deposition. Initially, the LHP NC solution is spin-casted on a substrate and the deposited film is exposed for t_{reac} time to the respective solution of cation halide in EtAc. The procedure is repeated two more times to produce films of the order of 100–150 nm. The last step includes the encapsulation of the film with a thin PMMA layer.

Table 1. List of samples under study, coded by the reaction time of the ligand washing step.

t_{reac} (s)	FAPbI ₃ NCs	CsPbBr ₃ NCs
0	FA0	Cs0
5	FA5	Cs5
10	FA10	Cs10
20	FA20	Cs20

films, corresponding roughly to NC aggregates formed by aggregation of four isolated NCs. The larger area Gaussian is peaked at ≈ 1000 or ≈ 2000 nm² depending on the reaction time. Increasing the reaction time from 5 to 20 s, results in an increase of the populations of the two Gaussians and eventually the dominance of the large area Gaussian. The findings of SEM are also supported by AFM microscopy shown in Figure 2i–l. AFM size distribution analysis cannot be performed reliably, but the growth of NC sintered grains can be indirectly inferred by the surface roughness that increases for the case of the presented images from ≈ 6 nm for FA0 to ≈ 24 nm for FA20; the complete evolution of surface roughness with ligand washing is shown in Table S1 (Supporting Information).

Interestingly, the morphology of the samples is influenced by the reaction environment. SEM and AFM images of films imposed to the same ligand washing in ambient conditions are included in Figure S2 (Supporting Information). Compared to samples prepared in the glove box, ligand washing in ambient conditions is more aggressive, producing reproducibly larger sintered domains with a particle distribution that resembles more a log-normal rather than a Gaussian function, as shown in Figure S3 (Supporting Information). AFM is also supportive of the SEM findings, with AFM images in Figure S2i–l (Supporting Information) and respected data at Table S1 (Supporting Information) providing evidence of increased surface roughness compared to glove box-treated samples. As elaborated later in the manuscript, in the presence of oxygen and humidity, the EtAc FAI solution is transformed to a more reactive agent being more invasive to the NC films.

Optical spectroscopy supports the microscopy data and provides further insight into the impact of ligand removal on the electronic states of the treated NCs. Figure 3a,b contains representative absorption spectra, while Figure 3c–f displays steady-state photoluminescence (PL) at 10 and 290 K, performed at the

FAPbI₃ NC sample series of Table 1, treated in and out of glove box. Raw data of the temperature-dependent steady state PL and time-resolved PL (TRPL) experiments are presented in Figures S4 and S5 (Supporting Information), respectively, while the main optical figures of merit are listed in Table S2 (Supporting Information). As ligand washing time increases, the PL peak and the band edge, redshift by as much as ≈ 60 meV evidencing a transition from isolated to sintered NCs, as seen in the summary plots in Figure 3g. Approximately 65% of this shift occurs in the F5 film, indicating that 5 s of washing by the EtAc:FAI formulation is sufficient to induce significant desorption of ligands and loss of confinement. For higher reaction times, the growth of the FAPbI₃ agglomerations results in suppression of the excitonic absorption and an overall increase of the optical density due to the increased material packing.

The impact of the washing time and processing environment is visible in the variable temperature PL spectra, displayed in Figure 3c–f for the samples processed in ambient and inert conditions at 10 and 290 K, respectively. At low temperatures, the intense single peak emission of the untreated FA0 NC film evolves into a red-shifted multi-component emission with an overall intensity gradually reducing with ligand washing time. The emission can be typically reproduced by a convolution of two or three Gaussian peaks, that are reasonably well resolved at cryogenic temperatures, as representatively displayed in Figure 3c,e, with complete lineshape analysis included in Figure S6 (Supporting Information). One of the peaks lies in the vicinity of the pristine NC emission and it is attributed to the excitonic emission from isolated NCs. As reaction time increases, ligand desorption promotes the aggregation of isolated NCs and the NC exciton emission peak quenches at the expense of the bulk-like red-shifted emission. The presence of weak NC exciton emission in the treated films indicates that a small fraction of the NCs remains relatively intact even after washing for up to 20 s. For such NCs, the small red-shift of the exciton PL peak by a few instead of several tens of meVs could be assigned to a combination of the change in dielectric environment and enhanced inter-NC coupling as partial ligand detachment occurs and NC packing increases. The obtained trends in FAPbI₃ NCs differ from those reported in the originally developed recipe by Zhao et al.^[14], where ligand washing combined with FAI treatment in CsPbI₃ NCs appears to keep fairly intact the great majority of the NCs, with the treatment mainly affecting the interparticle distance but not inducing pronounced NC aggregation. In a fraction of the treated films, additional luminescent components to the nanocrystal and

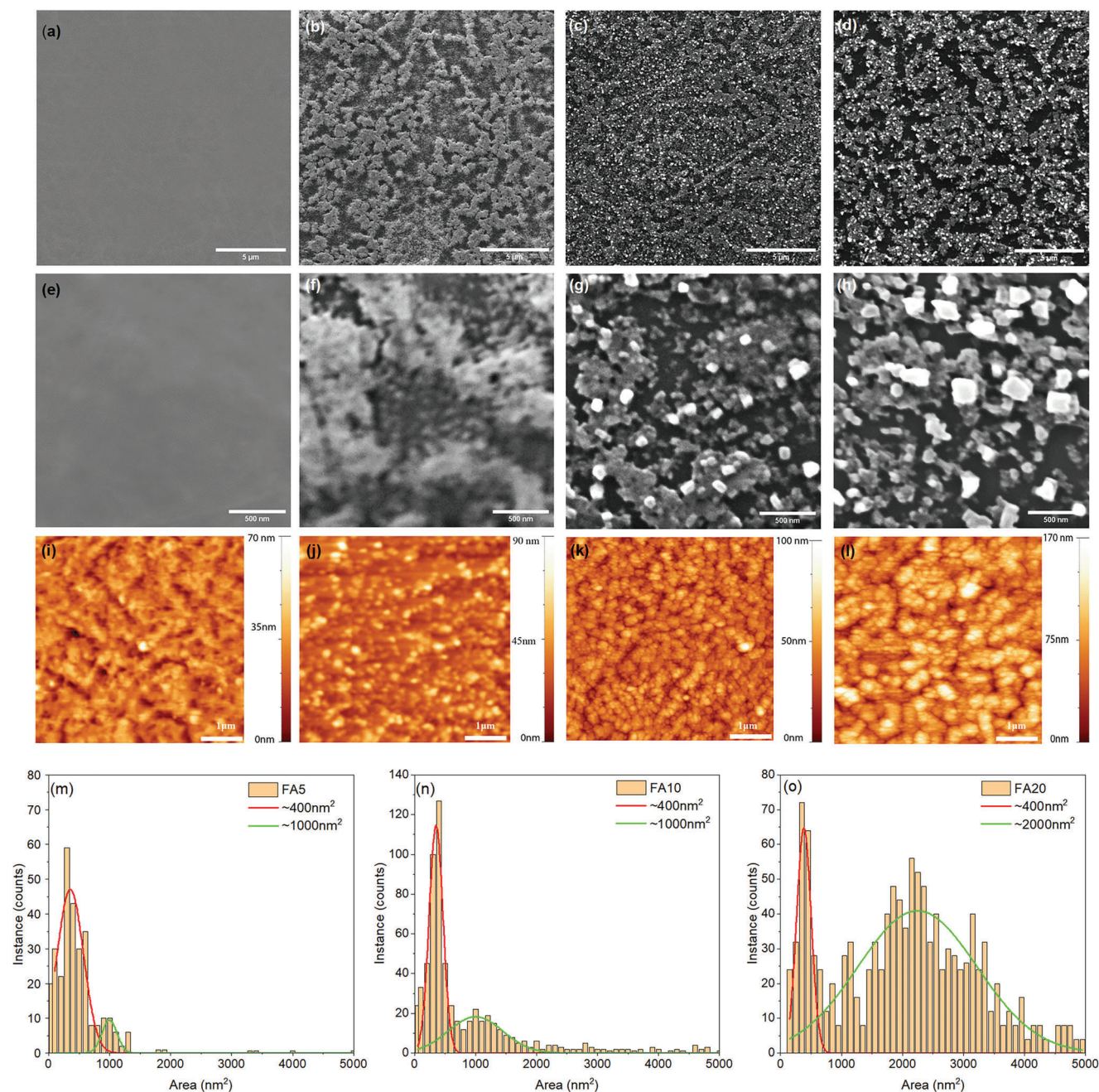


Figure 2. Low-resolution SEM images of a) FA0, b) FA5, c) FA10, and d) FA20 FAPbI₃ NCs films exposed to EtAc/FAI halide salt solution for 0, 5, 10, and 20 s respectively and prepared in inert conditions; the scale bar is 5 μ m. Higher resolution SEM images from the same e) FA0, f) FA5, g) FA10, and h) FA20 FAPbI₃ NCs films; the scale bar is 500 nm. AFM images of i) FA0, j) FA5, k) FA10, and l) FA20 FAPbI₃ NCs films; scale bar is 1 μ m. Particulate size analysis from SEM microscopy for m) FA5, n) FA10, and o) FA20 films.

bulk exciton emission emerge, with the most common case being displayed in Figure 3c and Figure S6e–h (Supporting Information), where a weak, blue-shifted Gaussian peak is visible. Evidence of the origin of such emission can be obtained using the high-resolution SEM images of Figure 2e,f. As ligand desorption on the FA10 and FA20 films becomes pronounced, the formation of more ordered platelet or rod-like crystals becomes visible. In such structures, quantum and dielectric confinement can ac-

count for the higher energy emission observed in the PL spectra. Etching of the NCs surface by the washing formulation could also produce this small sub-fraction of blue-emitting regions.

Despite the substantial NC structural transformation, the integrated luminescence of the film series treated within the glove box is not greatly affected by the application of the ligand exchange reaction for temperatures up to 200 K, while appreciable emission is recorded by the samples at room temperature. On

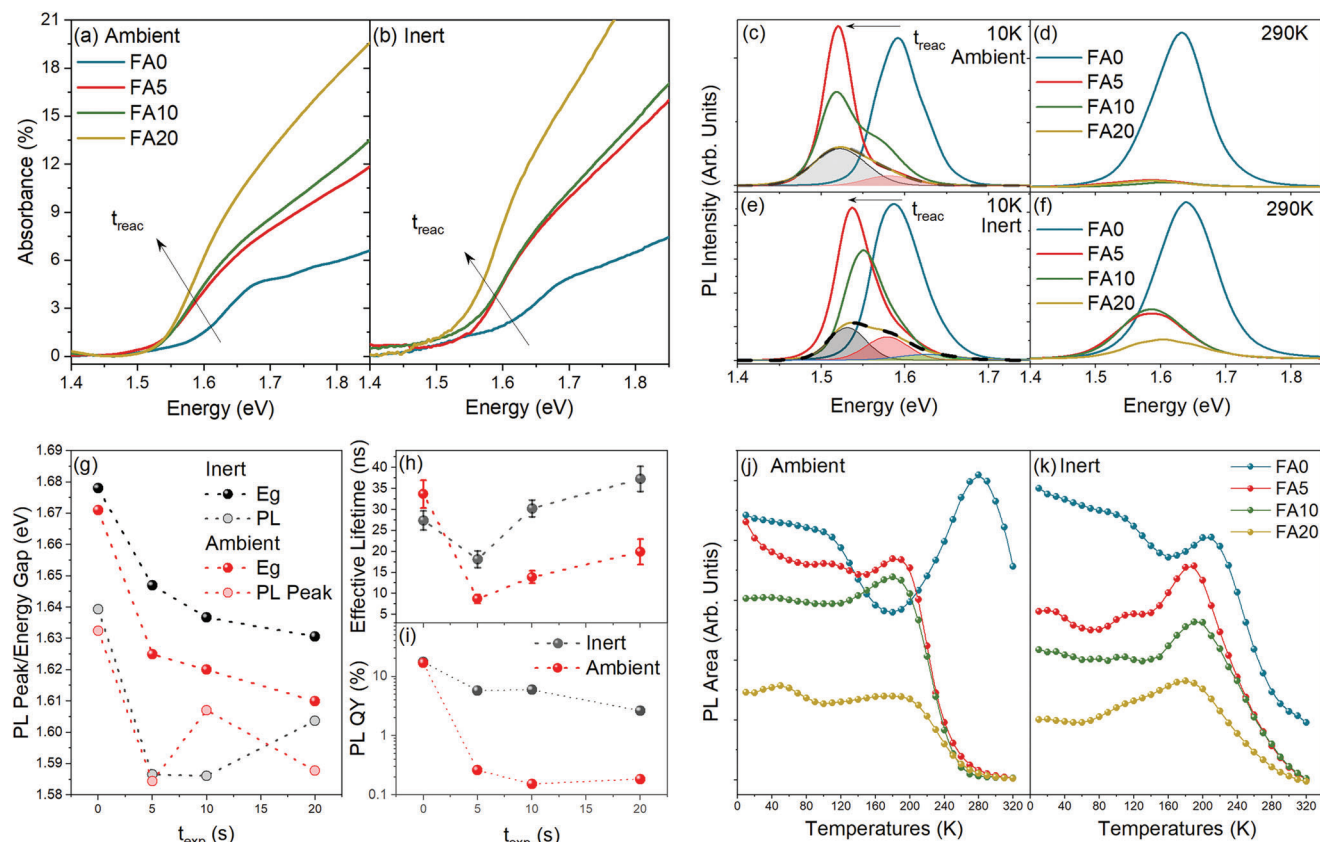


Figure 3. Optical absorption of FAPbI₃ NC films prepared under a) ambient and b) inert conditions. PL spectra at low (10K)/high (290K) temperatures of FAPbI₃ NC films prepared in c,d) ambient and e,f) inert conditions, respectively. PL peak position (open circles) and g) energy gap (solid spheres) for the samples under study. h) PL lifetime and i) QY for the two series. Integrated PL intensity as a function of film temperature processed in j) ambient and k) inert conditions.

the contrary, the emission from FAPbI₃ NC films prepared in air quenches by orders of magnitude compared to the pristine NC luminescence for temperatures above 200 K. The trend is reproduced in multiple sample series and indicates that upon removal of the oleic acid/oleilamine ligands in ambient conditions, non-radiative centers are formed that efficiently quench the exciton emission at elevated temperatures.

Further information on the origin of such defects can be obtained by a more precise examination of the lineshape of the variable temperature PL, presented in Figure 3j,k. Pristine samples in both cases show emission enhancement as the temperature is raised in the range of 160–250 K. Such behavior has been previously observed in inorganic and hybrid perovskite NC films and has been attributed to thermally-activated exciton de-trapping processes from surface traps that replenish the free NC exciton population thus increasing the emission.^[26] Previous work of some of the authors on CsPbBr₃ NCs²⁰ has shown that the de-trapping process is correlated with the depth of the surface traps, with more pronounced detrapping observed in well-passivated NC surfaces in which deep traps are largely eliminated. As shown in Figure 3j, as the ligand washing reaction time increases, such PL enhancement region suppresses, implying a respective increase of the surface trap energy. In other words, as ligand detachment increases, deeper defects are formed effectively local-

izing the excitons and suppressing their thermal escape to the NC electronic states manifold. It can be hypothesized that the formation of such traps is driven by the transformation of EtAc to acetic acid and methanol in the presence of humidity.^[27] Such biproducts react and corrode the NC surface creating deep trap states. This hypothesis is also supported by the effective PL lifetimes from the samples displayed in Figure 3h, where a lifetime enhancement with reaction time is attributed to slower recombination of excitons trapped at progressively deeper traps.

2.1.2. CsPbBr₃ NCs

CsPbBr₃ NCs were exposed to the same EtAc antisolvent formulation as FAPbI₃ NCs with subsequent treatment by CsBr to achieve ligand removal and healing of the surface dangling bonds, respectively. The study allows to evaluate the effectiveness and impact of the ligand exchange protocol on the more robust combination of inorganic CsPbBr₃ NCs decorated by the strongly bound DDAB/PbBr₂ capping ligands and further passivated via a PbBr₂ during post-synthetic ligand exchange.^[22] SEM and AFM images of the pristine Cs0 and the treated Cs5, Cs10, and Cs20 samples are displayed in Figure 4, demonstrating the appearance and growth of NC agglomeration with reaction time.

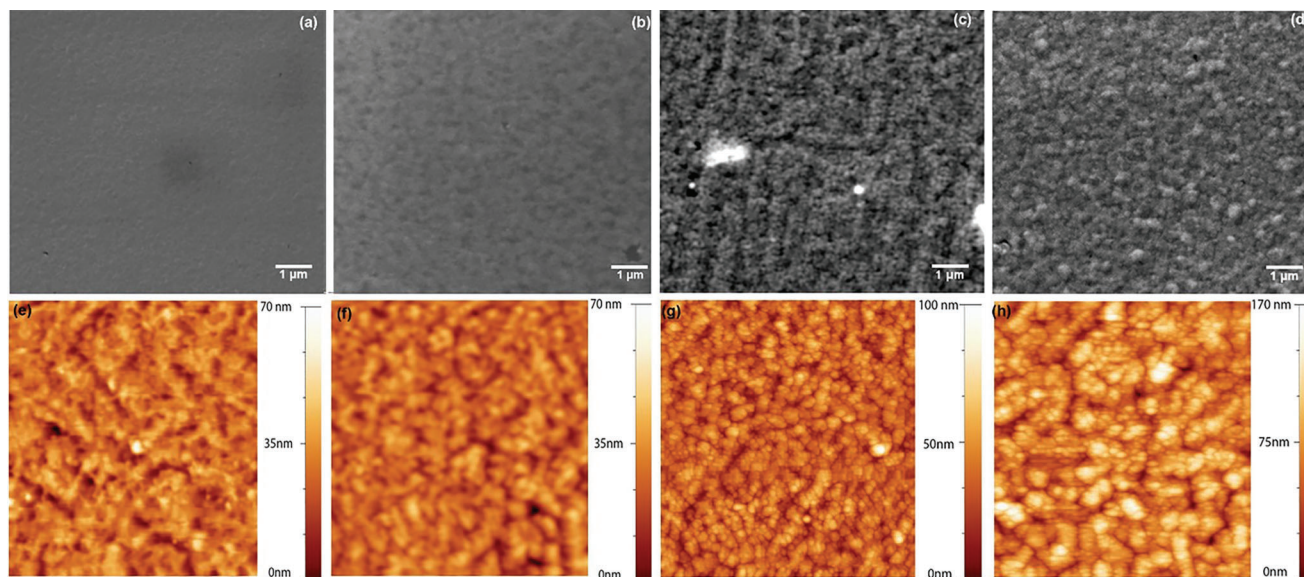


Figure 4. SEM images of a) Cs0, b) Cs5, c) Cs10, and d) Cs20, CsPbBr₃ NCs films exposed to EtAc/CsBr precursor solution prepared under inert conditions. AFM images of the same e) Cs0, f) Cs5, g) Cs10, and h) Cs20, CsPbBr₃ NC films.

Agglomerations of CsPbBr₃ NCs were found to be more than one order of magnitude larger than the larger areal population estimated in the FAPbI₃ NC series as seen in the particle analysis of Figure S7 (Supporting Information) and the cumulative Table S1 (Supporting Information) containing all structural data from the studied samples. This result seems counter-intuitive as the DDAB ligands are more strongly bound to the NC surface compared to the oleic acid/oleylamine molecules capping the FAPbI₃ NCs, which should result in reduced NC agglomeration. Based on the optical data presented later on, we hypothesize that the ligand removal of the DDAB ligands is partial, resulting in the packing of NCs within larger domains but allowing a large fraction of NCs to retain much of their nanostructured nature. Another interesting variation to the trends observed in the hybrid NC studies is that for CsPbBr₃ no systematic variation on the areal size and number of the NC agglomerated grains was observed upon applying the ligand washing reaction to films in inert or ambient conditions. Hence, it appears that the environment of the ligand removal reaction does not affect significantly the NC fusing process.

Absorption and comparative PL spectra at 10 and 290 K from the CsPbBr₃ NC films series, prepared at ambient and glove box conditions are presented in Figure 5a–f, respectively; the complete evolution of the PL spectra of each sample is included in Figure S8 (Supporting Information) and the main optical characteristics are listed in Table S3 (Supporting Information). Ligand washing results in the appearance and growth of lower energy states in absorption and PL extending to bulk CsPbBr₃ (≈ 2.3 eV).^[28] A defect origin for such tail states appears not to be compatible with the variable temperature PL spectra, as the opposite trend should have been observed with emissive defects becoming more pronounced at cryogenic temperatures. Some contribution from surface defects on the tail states cannot be ruled out, but we attribute the main contribution to recombination from electronic states of CsPbBr₃ NC agglomerated regions. The

loss of the ligand shell is further supported by the temperature evolution of PL intensity observed in Figure 5g, where exciton de-trapping promoted by the efficient surface passivation by the DDAB/PbBr₂ ligands is progressively suppressed. Nevertheless, removal of the DDAB/PbBr₂ ligands in the CsPbBr₃ NCs affects less the optical properties compared to the oleic acid/oleylamine desorption in the FAPbI₃ NC film series. This is evident by the emission quantum yield (QY) drop upon washing from ≈ 97 to $\approx 40\%$, shown in Figure 5h, for ambient treated samples. Such a drop is more than one order of magnitude smaller compared to the respective PL QY quenching induced by the ligand washing in the FAPbI₃ NCs. Furthermore, as observed in Figure 5i,j, a rather small redshift of the energy gap and a small increase of the PL FWHM is obtained while the PL peak energy appears to be largely unaffected by the ligand removal, indicating an incomplete loss of the ligand shell, as discussed earlier in the manuscript.

2.2. Electronic Conductivity

The impact of ligand removal on the electronic transport and conductivity properties of the films was studied via a combination of non-contact THz techniques and DC photoconductivity measurements performed in processed lateral devices. The optical experiments included THz time domain (TDS) and time-resolved (TRTS) spectroscopy, probing the THz frequency-dependent conductivity and the transient evolution of the THz transmission, respectively.^[29–31] Figure 6 presents the results of the TDS experiments on FAPbI₃ and CsPbBr₃ NC samples, prepared and treated in both ambient and glove box conditions. THz data are displayed only for the samples imposed to the ligand removal recipe, as in pristine NC samples the THz conductivity was found to be negligible, being hindered by the native ligands.

In TDS measurements shown in Figure 6, the real part of the conductivity assumes positive values, while the imaginary

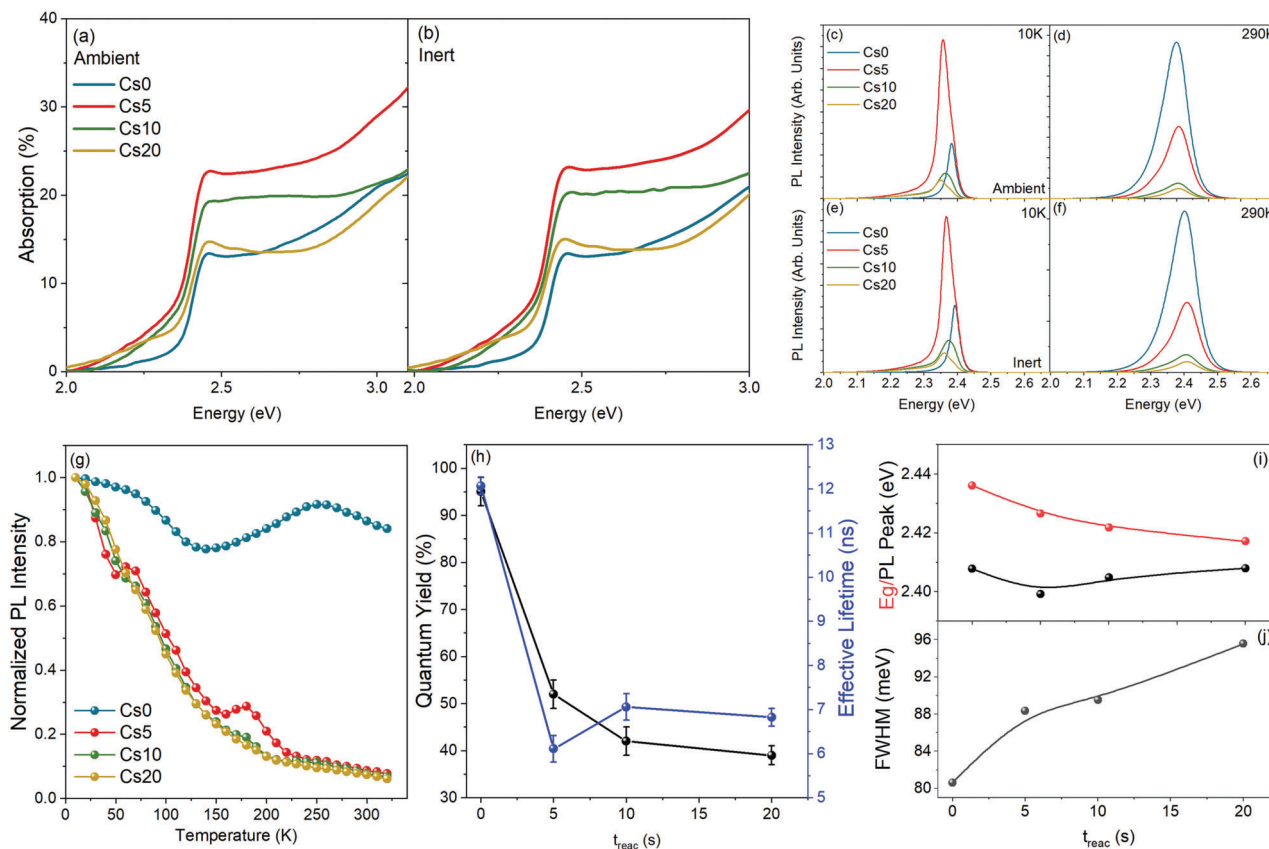


Figure 5. Absorption spectra for CsPbBr₃ NC films prepared under a) ambient and b) inert conditions. PL spectra at low (10K)/room temperature (290K) of CsPbBr₃ NC films prepared in c,d) ambient and e,f) inert conditions. g) Normalized integrated PL intensity as a function of temperature. h) PL QY (black dots) and effective lifetime (blue dots) as a function of reaction time. i) Eg (red dots) and PL peak (black dots) and j) full-width half maximum of PL lineshape as a function of t_{reac} .

part is negative for all studied samples. This is a characteristic behavior observed in perovskites of various dimensionalities and compositions^[32–37] when the average electron displacement is comparable to the material dimensions, as long as quantum confinement is not significant.^[38] Such a regime encompasses the relevant length scale range of transport of several tens to hundreds of nanometer-sized grains produced in the studied films. The behavior is typically described by the Drude–Smith model^[39] that introduces terms modifying the classical Drude model to accommodate for the effect of incomplete randomization of carrier momentum after collisions. In this model, the complex photoconductivity is given by Equation (1):

$$\Delta\sigma = \frac{Ne^2\tau/m^*}{(1 - i\omega\tau)} \left[1 + \frac{c}{1 - i\omega\tau} \right] \quad (1)$$

where N is the carrier density, e is the electron charge, m^* is the effective electron mass, τ is the scattering time of free carriers, ω is the angular frequency of the THz wave and c is a parameter that quantifies the fraction of the initial velocity of the electron that is retained after a collision. c can take values from 0 being the limit at the absence of backscattering to -1 denoting the bound of complete suppression of conductivity.^[39] In the data modeling, effective electron masses were taken as $0.15 m_0$ for CsPbBr₃^[40]

and $0.1 m_0$ for FAPbI₃^[41] with m_0 being the electron mass in vacuum.

For the case of the FAPbI₃ NC samples, it is observed that THz conductivity overall increases with the ligand removal time. However, the actual trends depend on the environmental conditions of sample processing.

In NC films prepared in ambient conditions, real and imaginary conductivity are maximized for the intermediate case of $t_{\text{reac}} = 10$ s, while in oxygen and humidity-free environment, a gradual and monotonic increase of conductivity is observed up to the maximum treatment time of 20 s. Importantly, conductivity on the latter samples assumes values larger by one order of magnitude compared to the respected values measured in ambient conditions, which is consistent with the optical spectroscopy findings, indicating a significantly more efficient formation of non-radiative centers upon NC aggregation in ambient conditions. For the FA samples fabricated in both types of environmental conditions, the persistence velocity, c , was found to be less than -0.5 , which indicates increased carrier localization. Specifically, in the ambient environment, c ranged from -0.78 to -0.68 , and for inert conditions, from -0.79 to -0.82 as depicted in Table S4 (Supporting Information). As more ligands are removed, larger grains are formed, and scattering becomes less efficient reducing the absolute value of the parameter c and increasing the average

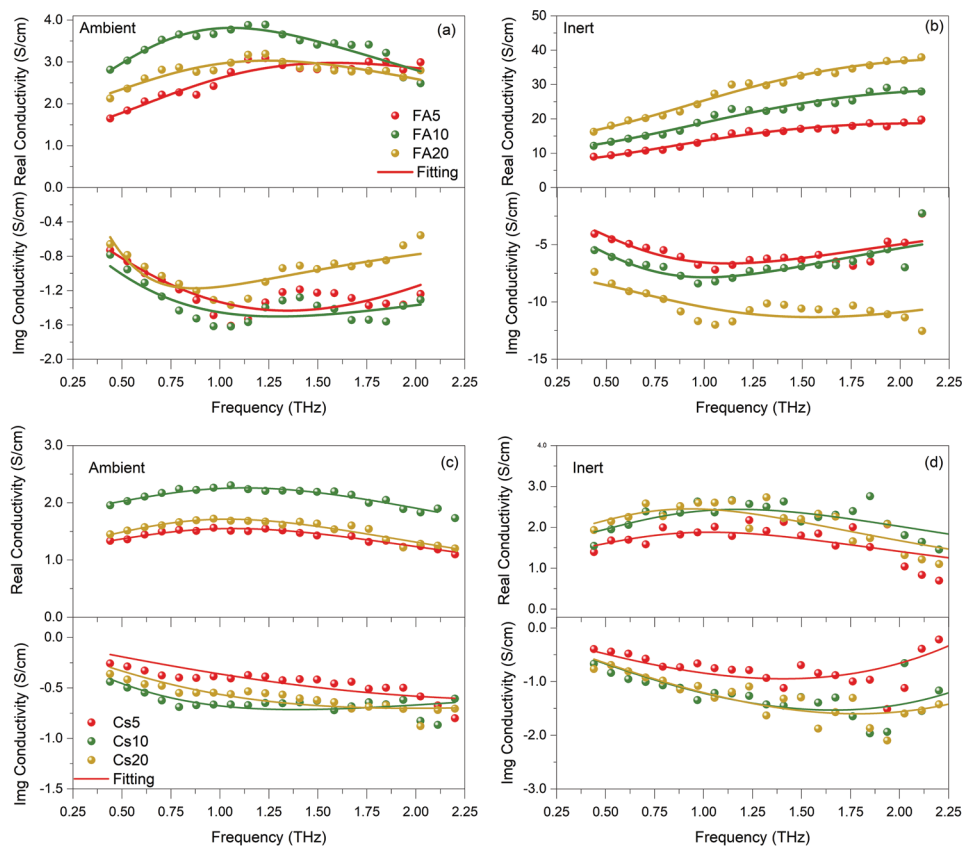


Figure 6. Real conductivity (top) and imaginary conductivity (bottom) for a) ambient and b) inert prepared FAPbI₃ NC samples. The solid lines represent the fitting of the data with the Drude–Smith model. Real conductivity (top) and imaginary conductivity (bottom) for c) ambient and d) inert prepared CsPbBr₃ NC films. All data were acquired using a pump fluence of 38 $\mu\text{J cm}^{-2}$.

scattering time τ . The reduced backscattering, i.e., smaller absolute values of c and larger scattering times τ observed in the ambient prepared films compared to glove box treated samples agrees with the more extensive aggregation of NCs in the presence of oxygen and moisture evidenced by the structural measurements described previously. Identical experiments were performed on the CsPbBr₃ NCs samples. The TDTS experiments reveal a slight increase in conductivity for the samples that were prepared in a controlled environment (Figure 6c,d). The persistence velocity and the scattering time parameter values appear largely insensitive to the ligand washing time and the reaction environment as shown in Table S4 (Supporting Information). Overall, the impact of ligand washing time is less significant compared to the case of FAPbI₃ NCs.

Representative data from the TRTS experiments are displayed in Figure 7. The signal amplitude at $t = 0$ is proportional to the THz conductivity and follows the respective trends obtained in the TDTS experiments of Figure 6 namely: i) higher conductivity for FAPbI₃ NC samples prepared in the glove box, ii) monotonic increase of the conductivity with ligand washing time in the inert produced films compared to ambient treated samples in which conductivity reduces when washed for >10 s, iii) continuous increase of conductivity for inert and ambient treated CsPbBr₃ NC samples but overall smaller signal compared to the FAPbI₃ material. Importantly the TRTS measurements can provide insight

on charge recombination dynamics processes taking place after photoexcitation. The decays recorded from all samples require fitting by triple-exponential functions, yielding for both FAPbI₃ NC and CsPbBr₃ samples, a short decay constant τ_1 in the range of 5–10 ps, an intermediate decay τ_2 at 20 to 30 ps and a significantly slower component τ_3 ranging from 140 to 220 ps. What changes between CsPbBr₃ and FAPbI₃ NC samples is the relative amplitude of each of the three decays. Based on previous work of some of the authors on transient spectroscopy of such NCs across similar type of photoexcitation densities^[42,43] the first two decay times could be associated with carrier relaxation via phonons that is retarded by effects such as hot phonon bottleneck and Auger heating or multicarrier recombination via the Auger mechanism; the τ_3 timescales seem compatible with radiative recombination and/or carrier trapping. In the case of CsPbBr₃ films, the fluence exceeds the ASE threshold of CsPbBr₃ NCs (30 $\mu\text{J cm}^{-2}$),^[43] so one of the decays could also be associated with stimulated emission.

In order to further investigate the nature of the carrier recombination processes as a function of ligand washing time, the excitation-dependent THz transient data are simulated with the following rate equation model in Equation (2):

$$\frac{dn(t)}{dt} = -k_1 n - k_2 n^2 - k_3 n^3 \quad (2)$$

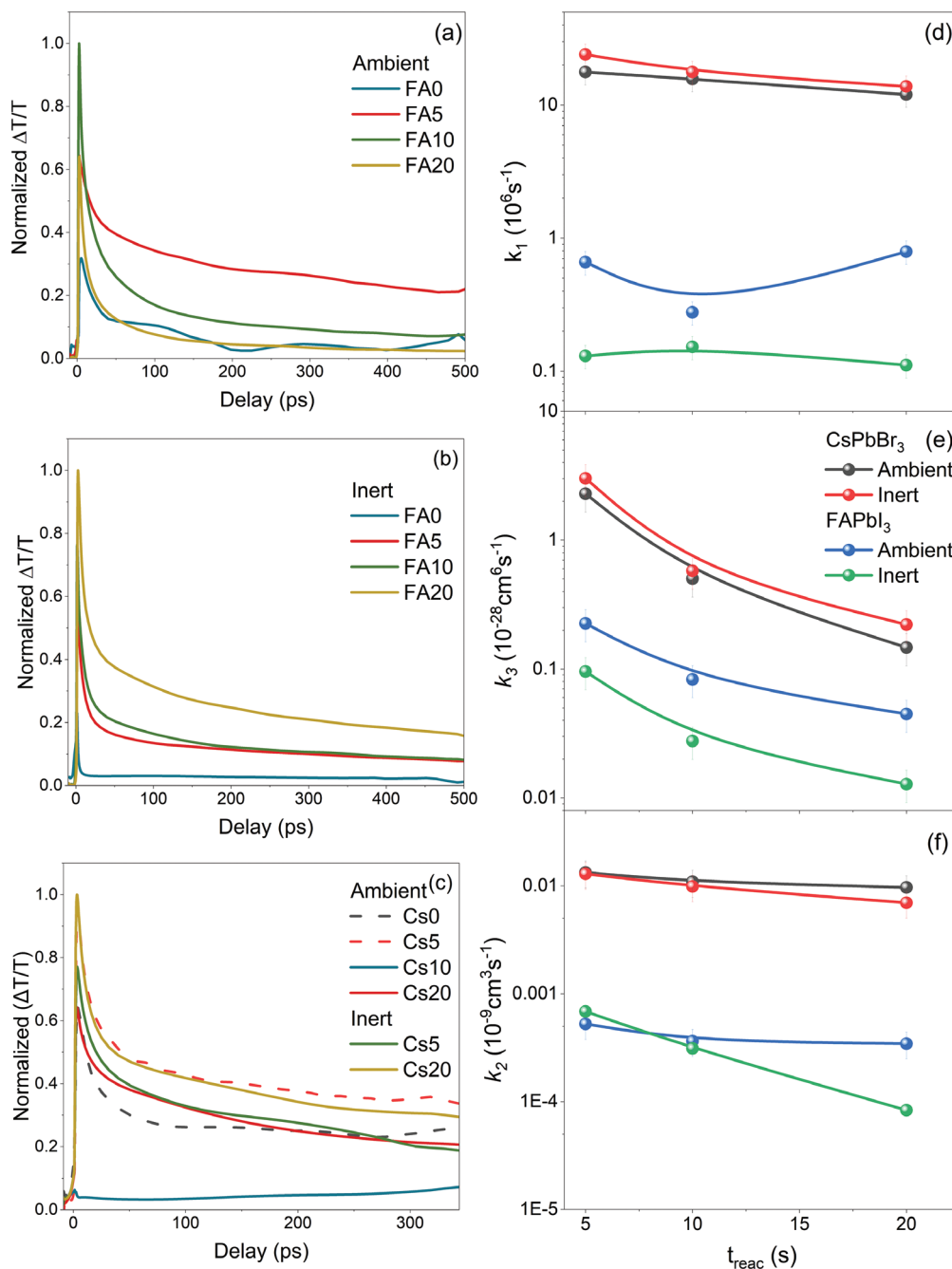


Figure 7. Normalized time-resolved THz signal for a) ambient and b) inert prepared FAPbI₃, and c) for all CsPbBr₃ NC films. d) Monomolecular, e) bi-Molecular, and f) Auger coefficients extracted by the model described by Equation (3).

where $n(t)$ is the free carrier charge density, k_1 is the monomolecular recombination coefficient, k_2 is the bimolecular recombination coefficient and k_3 is the Auger coefficient. The model assumes unbound electrons and holes as neutral excitons do not directly contribute to the THz conductivity. The coefficient values extracted from the fittings are displayed in Figure 7d–f as a function of ligand washing time. Monomolecular recombination is dominated by trap-assisted carrier recombination, while the main contribution to the bimolecular recombination is expected to be the radiative recombination of electron–hole

pairs. For FAPbI₃, the fits for the glove box films yields k_1 values consistently lower than the respective rate constants in the air-treated films, in line with the enhanced non-radiative recombination evidenced by the PL studies and the reduced THz conductivity of the latter samples. For the inert samples, trapping appears fairly independent on the ligand washing time while for ambient films trapping shows a non-monotonic variation reflecting the respective variation of the THz conductivity, i.e., the conductivity (trapping), increases (decreases) for ligand removal reaction time up to 10 s and subsequently it

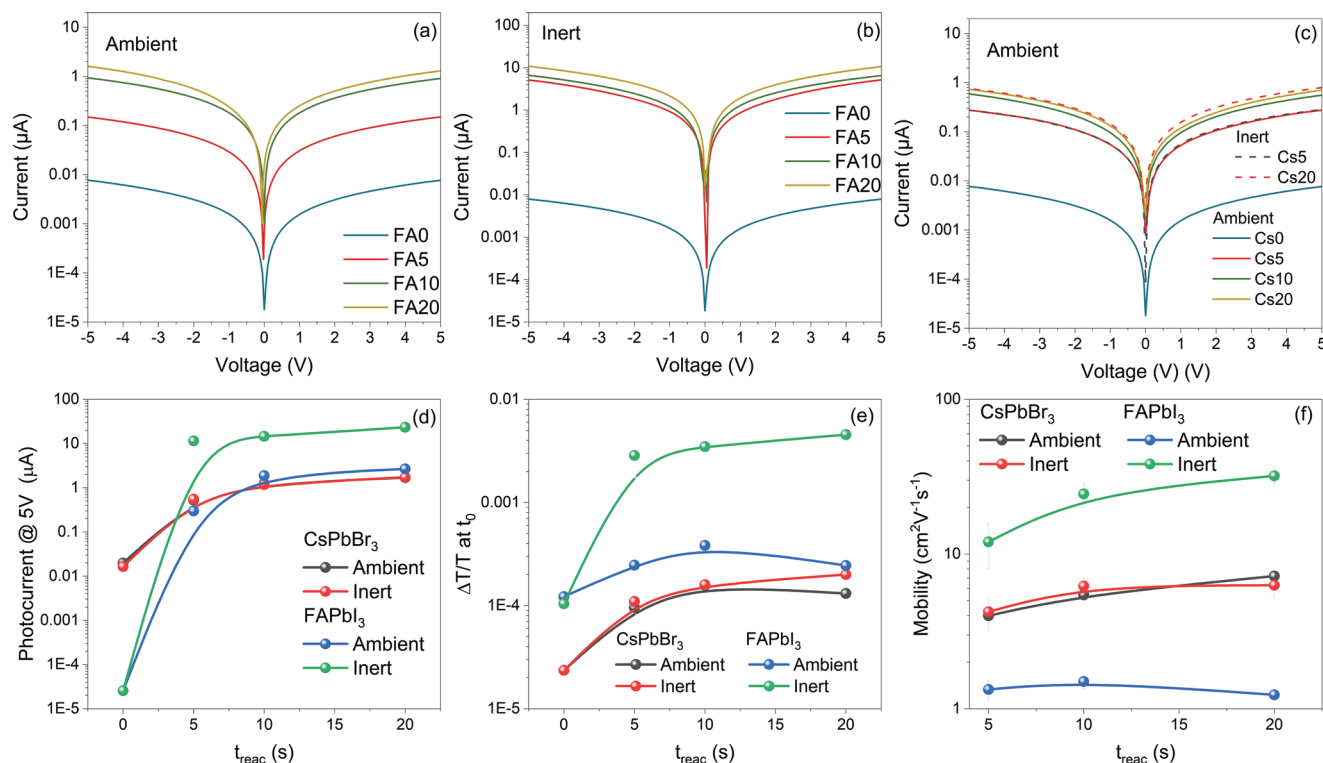


Figure 8. Photoconductivity signal (photocurrent) for a) ambient, b) inert prepared FAPbI₃, and c) CsPbBr₃ NC films excited at $\lambda = 410$ nm and power density of 32 mW cm^{-2} . d) Maximum photocurrent at 410 nm , 32 mW cm^{-2} excitation/ 5 V bias. e) THz differential signal at t_0 and f) extracted mobility from Equation (4) as a function of t_{reac} for all samples under study.

decreases (increases) for more extensive ligand stripping. The bimolecular recombination coefficient k_2 and the Auger rate constant k_3 exhibit qualitatively similar trends, namely reducing as ligand washing time increases, however, the quenching in the Auger coefficient is significantly more severe. The reduction of the two rate constants is predominantly attributed to the loss of confinement as NC sinter/agglomerate upon desorption of the ligands. The increase of electronic communication and the faster electron and hole transport as the ligand shell is removed, also compete with the two recombination mechanisms. For the CsPbBr₃ NC samples, all recombination coefficients reduce with ligand washing, in a very similar fashion for samples fabricated in and out of glove box, consistent with the morphological and spectroscopic results. As in the case of FAPbI₃ NC samples, ligand desorption has a higher impact on Auger recombination, owing to its strong dependence to confinement.

Figure 8a–c contains photoconductivity data from lateral ITO-NC-ITO devices incorporating in the active region the ambient and inert treated FAPbI₃ and CsPbBr₃ films. The results show a monotonic increase of the photocurrent with the reaction time for both CsPbBr₃ and FAPbI₃ NC films, however, the improvement in the latter samples is larger due to the more efficient depletion of the NC ligand shell upon washing. A quantitative comparison between the THz conductivity and photoconductivity experiments is challenging due to the different experimental conditions of the two experiments. However, the qualitative similar behavior of the evolution of the THz and photocurrent signals with ligand washing times is evident in Figure 8d,e, displaying

the maximum photocurrent at bias of 5 V upon photoexcitation in the violet (410 nm). Figure 8f displays the maximum THz carrier mobility as a function of ligand washing time for all studied samples. The mobility was calculated by Equation (3):

$$\mu = \frac{S}{ne} \quad (3)$$

where S is the THz conductivity at $\approx 1.2 \text{ THz}$, where the maximum signal was observed for most of the studied films, n is the carrier density, and e is the electron charge. Mobility shows the same trends with the photocurrent and the THz signal, namely: i) increases with washing time for all samples apart from the most heavily (FA20), air-treated FAPbI₃ NC films. ii) FAPbI₃ NC films prepared in an ambient environment show significantly lower mobility values than those in the inert prepared samples. iii) CsPbBr₃ NC samples show nearly identical mobilities when prepared under inert and ambient conditions.

3. Conclusion

In summary, a comprehensive study was carried out to understand the influence of a ligand removal procedure based on ethyl acetate and simultaneous cation halide salt passivation, repeated to build a layer-by-layer perovskite NC assembly. The protocol was applied to $\approx 10\text{--}12 \text{ nm}$ CsPbBr₃ and FAPbI₃ NCs to produce electronically active films. Variables of the study included the time exposure of the materials to the washing formulation and

the environmental conditions in which the reaction took place. Microscopy revealed that even a moderate exposure of the material to the precursor solutions leads to aggregation of the FAPbI₃ NCs. For such NCs the ligand washing appears more aggressive at ambient conditions resulting in more extended aggregation as well as more pronounced non-radiative recombination compared to films treated in controlled glove box conditions. For CsPbBr₃ NCs, the reaction environment was found to play an insignificant role on the structural and optical properties of the treated films. Interestingly electron microscopy indicates the formation of larger domains in the inorganic NCs compared to the FAPbI₃ sintered regions, however, the optical properties and the emission efficiency of the former are significantly less affected by the ligand washing process compared to the FA-based solids.

The different impact of ligand desorption in the two systems is attributed to: i) the weaker surface bonding of the oleic acid/oleylamine molecules in the FAPbI₃ NCs compared to the binding affinity of the DDAB complexes in CsPbBr₃ NCs¹⁷, making them more prone to desorption upon treatment. DDAB has been shown^[17,45] to be able to penetrate and bind strongly onto the CsPbBr₃ NC surfaces, inhibiting NC aggregation and shape or size alteration while exhibiting a higher barrier for ligand adsorption/desorption compared to conventional ligands. As discussed in the manuscript, when the reaction occurs in air, oxygen promotes partial transformation of the EtAc-based washing formulation to acetic acid. The corroding action of the acid is more intense in the FAPbI₃ NC system, as the surface of such NCs is much more ligand-depleted and less protected compared to that of the treated CsPbBr₃ NCs. ii) Oxygen and air are expected to have a higher impact on the chemical nature of the FAI-EtAc formulation compared to the CsBr-EtAc counterpart. Iodine has a higher tendency to undergo oxidation reactions compared to bromine, especially in the specific compounds used, where iodine forms a salt with the more volatile formamidinium compared to the less reactive and more stable CsBr salt. It is thus plausible that air affects much more the more volatile FAI-EtAc solution.

The important impact of the ligand detachment on the electrical properties of the samples is probed by THz spectroscopy and photoconductivity experiments performed in films and lateral ITO-NC-ITO devices. Such experiments provide conclusive evidence that the ligand removal improves substantially the conductivity properties of the treated films; for the case of the glove box prepared samples, the improvement is monotonic up to 20 s of washing while more aggressive ligand removal results in material degradation. Via transient THz measurements and by employing the Drude–Smith type of modeling, monomolecular, biomolecular and Auger coefficients are extracted as a function of the ligand washing time with radiative (biomolecular) and Auger recombination suppressing with ligand removal due to the loss of carrier confinement. The maximum THz mobility of each system was estimated, with glove box prepared FAPbI₃ NC samples mobility reaching values as high as $\approx 30 \text{ V}^{-1}\text{s}^{-1}\text{cm}^2$ compared to ambient FA-based films of $\approx 1 \text{ V}^{-1}\text{s}^{-1}\text{cm}^2$ and CsPbBr₃ NC films of $\approx 6 \text{ V}^{-1}\text{s}^{-1}\text{cm}^2$. Overall, the work indicates that relatively simple, chemical ligand washing protocols can have a highly beneficial and quite reproducible effect in the conductivity properties of LHP NC solids; however, the success of such treatments is criti-

cally dependent on comprehensive studies that can tailor the processes to the specific NC-ligand system of interest and evaluate and optimize the impact of parameters, such as the reaction time and the reaction environment.

4. Experimental Section

Material Fabrication: CsPbBr₃ NCs capped with DDAB-PbBr₂ were synthesized according to the Ref. [40].

FAPbBr₃ NCs capped with oleic acid-oleylamine were synthesized according to the Ref. [40].

Film/Device Fabrication: Films under study were fabricated via spin coating under inert or ambient conditions, from material solutions with concentration of $\approx 20 \text{ g L}^{-1}$ in toluene. The substrates were initially cleaned with nitric acid (HNO₃), rinsed with de-ionized water, boiled in n-butyl acetate, followed by sonication in acetone for 20 min, and rinsed with isopropanol. 70 μL of solution was spin coated at 1500 rpm for 60 s followed by a drying step at 4000 rpm for 20 s. After casting the NC layer, 70 μL of saturated FAI for FAPbI₃ and CsBr for CsPbBr₃ NCs in EtAc solution, was deposited on the layer and dried with spinning at 4000 rpm for 60 s. The exposure time of the films to their respective precursor solution was varied between 0 and 20 s as described in the manuscript. The whole procedure was repeated three times for each film. To protect the films, encapsulation by dynamic spinning of 30 mg mL^{-1} PMMA in toluene solution at 5000 rpm for 60 s was performed. For the fabrication of lateral devices, 50 μm channel interdigitated ITO substrates (Ossila) were used as substrates following the same procedure for the film deposition and treatment.

Microscopy: The morphological characterization of the samples was carried out by scanning electron microscopy (SEM) and atomic force microscopy (AFM) techniques. For SEM a Tescan Vega LSU microscope was employed at 20 kV and various magnifications ranging from 10 to 80k. AFM was executed by a Multiview 4000 SPM/AFM/NSOM confocal multi-probe system (Nanonics). The system consists of two probes and a piezo scanning sample stage, which can be independently controlled, allowing to perform scans up to $85 \times 85 \mu\text{m}$ area in a non-contact mode.

Optical Spectroscopy: Absorption spectra were obtained by a Perkin Elmer Lambda 1050 spectrophotometer equipped with a three-detector module covering the 300–3300 nm spectral range. Steady-state photoluminescence (PL) was carried out using a 0.35 m FluoroLog FL3 Horiba Jobin Yvon spectrofluorometer. The samples were excited by a 405 nm Oxixus laser diode at relatively low powers ($< 5 \text{ mW}$) to exclude multi-exciton and photo-charging effects. The acquired spectra were corrected according to the absorbance of each film at the excitation wavelength to account for thickness variations between films. PL quantum yield (QY) experiments were conducted in a LabSphere 4-inch integrating sphere coupled to an i750 Princeton spectrometer equipped with a 256×1024 pixel CCD camera via an optical fiber bundle. Samples were excited with a 405 nm Oxixus laser diode at low powers ($< 5 \text{ mW}$). For the PL QY experiments, the integrating sphere-based method described by J. de-Mello et. al^[44] was used. The method was based on the use of three sphere configurations that include an empty sphere reference, a scheme with the sample in place and the laser beam directed onto the sphere wall to measure indirect emission from the sample and the main configuration in which the laser beam was directed onto the sample to acquire the direct NC emission.

Time-resolved photoluminescence (TR-PL) was measured on the FL3 spectrometer, using a monochromator-based time-correlated single photon counting (TCSPC) method. The samples were excited by a 405 nm NanoLED laser diode with pulse width of $\approx 80 \text{ ps}$, operating at 100 KHz. The data were acquired at different spots on each sample for spatial averaging. The PL decays were obtained while monitoring the peak emission within a bandwidth of $\approx 3 \text{ nm}$. The effective transient PL lifetime τ_{eff} was calculated via the relation below Equation (4):

$$\tau_{\text{eff}} = \frac{\sum_i A_i \tau_i^2}{\sum_i A_i \tau_i} \quad (4)$$

where τ_i is the decay times extracted from the exponential fits of the PL transients and A_i the corresponding decay amplitudes.^[45] All data except the absorption and the PL QY were acquired with samples placed in vacuum conditions ($\sim 10^{-6}$ mbar) using a closed cycle Janis cryostat that allowed temperature-dependent PL experiments in the range of 10–340 K.

THz Spectroscopy: The experimental setup used for the THz measurements consisted of a Spectra-Physics Tsunami Ti:Sapphire oscillator and a Spitfire amplifier to generate output 100 fs pulses at 800 nm, with a repetition rate of 1 KHz. The pulses were guided to a conventional TRTS experimental apparatus.^[46] The samples were excited by 400 nm pulses created by second harmonic frequency mixing with energies that can reach up to 150 $\mu\text{J pulse}^{-1}$. The THz pulses were generated by nonlinear rectification in a 0.5 mm $\langle 110 \rangle$ ZnTe nonlinear crystal. Detection was achieved via free-electrooptic sampling using an additional 0.5 mm $\langle 110 \rangle$ ZnTe crystal. TDTS measurements were used to extract the photoconductivity and mobility in the THz region as a function of ligand washing time. During the presented experiments, the samples were illuminated by pump pulses at 400 nm with fluence of 38 $\mu\text{J cm}^{-2}$.

Photoconductivity: To measure the photoconductivity of lateral devices a Keithley 2461 source meter was employed. The samples were placed under a Zeiss epifluorescence microscope and excited with a quasi-monochromatic beam of 410 ± 20 nm with a power density of 32 mW cm^{-2} . For each measurement, to ensure device isolation from neighboring devices, spacing grooves were produced on the deposited material.

Supporting Information

Supporting Information is available from the Wiley Online Library or from the author.

Acknowledgements

P.P. and M.S. contributed equally to this work. This work was financially supported by the Research and Innovation Foundation of Cyprus under the “NEW STRATEGIC INFRASTRUCTURE UNITS-YOUNG SCIENTISTS” Programme (Grant Agreement No. “INFRASTRUCTURES/1216/0004”, Acronym “NANOSONICS”). M.S. was financially supported by the Research and Innovation Foundation of Cyprus under Grant Agreement No. “OPPORTUNITY/MSCA/0024”, Acronym “FastBind”.

Conflict of Interest

The authors declare no conflicts of interest.

Data Availability Statement

The data that support the findings of this study are available from the corresponding author upon reasonable request.

Keywords

lead halide perovskites, ligands, nanocrystals, photoconductivity, photoluminescence, THz spectroscopy

Received: June 25, 2023

Revised: September 11, 2023

Published online: November 10, 2023

- [1] M. V. Kovalenko, L. Protesescu, M. I. Bodnarchuk, *Science* **2017**, 358, 745.

- [2] Q. A. Akkerman, G. Rainò, M. V. Kovalenko, L. Manna, *Nat. Mater.* **2018**, 17, 394.
 [3] A. Dey, J. Ye, A. De, E. Debroye, S. K. Ha, E. Bladt, A. S. Kshirsagar, Z. Wang, J. Yin, Y. Wang, L. N. Quan, F. Yan, M. Gao, X. Li, J. Shamsi, T. Debnath, M. Cao, M. A. Scheel, S. Kumar, J. A. Steele, M. Gerhard, L. Chouhan, K. Xu, X.-G. Wu, Y. Li, Y. Zhang, A. Dutta, C. Han, I. Vincon, A. L. Rogach, et al., *ACS Nano* **2021**, 15, 10775.
 [4] K. Chen, Q. Zhong, W. Chen, B. Sang, Y. Wang, T. Yang, Y. Liu, Y. Zhang, H. Zhang, *Adv. Funct. Mater.* **2019**, 29, 1900991.
 [5] J. Shi, F. Li, Y. Jin, C. Liu, B. Cohen-Kleinstein, S. Yuan, Y. Li, Z.-K. Wang, J. Yuan, W. Ma, *Angew. Chem.* **2020**, 132, 22414.
 [6] D. Jia, J. Chen, M. Yu, J. Liu, E. M. J. Johansson, A. Hagfeldt, X. Zhang, *Small* **2020**, 16, 2001772.
 [7] L. M. Wheeler, E. M. Sanehira, A. R. Marshall, P. Schulz, M. Suri, N. C. Anderson, J. A. Christians, D. Nordlund, D. Sokaras, T. Kroll, S. P. Harvey, J. J. Berry, L. Y. Lin, J. M. Luther, *J. Am. Chem. Soc.* **2018**, 140, 10504.
 [8] M. Hao, Y. Bai, S. Zeiske, L. Ren, J. Liu, Y. Yuan, N. Zarrabi, N. Cheng, M. Ghasemi, P. Chen, M. Lyu, D. He, J.-H. Yun, Y. Du, Y. Wang, S. Ding, A. Armin, P. Meredith, G. Liu, H.-M. Cheng, L. Wang, *Nat. Energy* **2020**, 5, 79.
 [9] L. N. Quan, R. Quintero-Bermudez, O. Voznyy, G. Walters, A. Jain, J. Z. Fan, X. Zheng, Z. Yang, E. H. Sargent, *Adv. Mater.* **2017**, 29, 1605945.
 [10] E. M. Sanehira, A. R. Marshall, J. A. Christians, S. P. Harvey, P. N. Ciesielski, L. M. Wheeler, P. Schulz, L. Y. Lin, M. C. Beard, J. M. Luther, *Sci. Adv.* **2017**, 3, eaao4204.
 [11] J. Y. Kim, J.-W. Lee, H. S. Jung, H. Shin, N.-G. Park, *Chem. Rev.* **2020**, 120, 7867.
 [12] A. Swarnkar, A. R. Marshall, E. M. Sanehira, B. D. Chernomordik, D. T. Moore, J. A. Christians, T. Chakrabarti, J. M. Luther, *Science* **2016**, 354, 92.
 [13] X. Ling, S. Zhou, J. Yuan, J. Shi, Y. Qian, B. W. Larson, Q. Zhao, C. Qin, F. Li, G. Shi, C. Stewart, J. Hu, X. Zhang, J. M. Luther, S. Duhm, W. Ma, *Adv. Energy Mater.* **2019**, 9, 1900721.
 [14] Q. Zhao, A. Hazarika, X. Chen, S. P. Harvey, B. W. Larson, G. R. Teeter, J. Liu, T. Song, C. Xiao, L. Shaw, M. Zhang, G. Li, M. C. Beard, J. M. Luther, *Nat. Commun.* **2019**, 10, 2842.
 [15] F. Li, S. Zhou, J. Yuan, C. Qin, Y. Yang, J. Shi, X. Ling, Y. Li, W. Ma, *ACS Energy Lett.* **2019**, 4, 2571.
 [16] Q. Zhao, A. Hazarika, X. Chen, S. P. Harvey, B. W. Larson, G. R. Teeter, J. Liu, T. Song, C. Xiao, L. Shaw, M. Zhang, G. Li, M. C. Beard, J. M. Luther, *Nat. Commun.* **2019**, 10, 2842.
 [17] M. Hao, Y. Bai, S. Zeiske, L. Ren, J. Liu, Y. Yuan, N. Zarrabi, N. Cheng, M. Ghasemi, P. Chen, M. Lyu, D. He, J.-H. Yun, Y. Du, Y. Wang, S. Ding, A. Armin, P. Meredith, G. Liu, H.-M. Cheng, L. Wang, *Nat. Energy* **2020**, 5, 79.
 [18] Q. A. Akkerman, M. Gandini, F. Di Stasio, P. Rastogi, F. Palazon, G. Bertoni, J. M. Ball, M. Prato, A. Petrozza, L. Manna, *Nat. Energy* **2017**, 2, 16194.
 [19] C. C. Stoumpos, C. D. Malliakas, M. G. Kanatzidis, *Inorg. Chem.* **2013**, 52, 9019.
 [20] L. Protesescu, S. Yakunin, S. Kumar, J. Bär, F. Bertolotti, N. Masciocchi, A. Guagliardi, M. Grotevent, I. Shorubalko, M. I. Bodnarchuk, C.-J. Shih, M. V. Kovalenko, *ACS Nano* **2017**, 11, 3119.
 [21] M. Liu, Z. Li, W. Zheng, L. Kong, L. Li, *Front Mater* **2019**, 6, 306.
 [22] M. I. Bodnarchuk, S. C. Boehme, S. Ten Brinck, C. Bernasconi, Y. Shynkarenko, F. Krieg, R. Widmer, B. Aeschlimann, D. Günther, M. V. Kovalenko, I. Infante, *ACS Energy Lett.* **2019**, 4, 63.
 [23] D. Yang, X. Li, H. Zeng, *Adv. Mater. Interfaces* **2018**, 5, 1800260.
 [24] C. Zheng, C. Bi, F. Huang, D. Binks, J. Tian, *ACS Appl. Mater. Interfaces* **2019**, 11, 25410.
 [25] W. Chen, X. Tang, P. Wangyang, Z. Yao, D. Zhou, F. Chen, S. Li, H. Lin, F. Zeng, D. Wu, K. Sun, M. Li, Y. Huang, W. Hu, Z. Zang, J. Du, *Adv. Opt. Mater.* **2018**, 6, 1800007.

- [26] A. Manoli, P. Papagiorgis, M. Sergides, C. Bernasconi, M. Athanasiou, S. Pozov, S. Choulis, M. Bodnarchuk, M. Kovalenko, A. Othonos, G. Itkos, *ACS Appl. Nano Mater.* **2021**, 4, 5084.
- [27] L. M. Wheeler, E. M. Sanehira, A. R. Marshall, P. Schulz, M. Suri, N. C. Anderson, J. A. Christians, D. Nordlund, D. Sokaras, T. Kroll, S. P. Harvey, J. J. Berry, L. Y. Lin, J. M. Luther, *J. Am. Chem. Soc.* **2018**, 140, 10504.
- [28] M. Sebastian, J. A. Peters, C. C. Stoumpos, J. Im, S. S. Kostina, Z. Liu, M. G. Kanatzidis, A. J. Freeman, B. W. Wessels, *Phys. Rev. B* **2015**, 92, 235210.
- [29] F. J. García-Vidal, J. M. Pitarke, J. B. Pendry, *Phys. Rev. Lett.* **1997**, 78, 4289.
- [30] C. A. S. Matthew, C. Beard, G. M. Turner, *J. Phys. Chem. B* **2002**, 106, 7146.
- [31] E. Hendry, F. Wang, J. Shan, T. F. Heinz, M. Bonn, *Phys. Rev. B* **2004**, 69, 081101.
- [32] C. La-O-Vorakiat, T. Salim, J. Kadro, M.-T. Khuc, R. Haselsberger, L. Cheng, H. Xia, G. G. Gurzadyan, H. Su, Y. M. Lam, R. A. Marcus, M.-E. Michel-Beyerle, E. E. M. Chia, *Nat. Commun.* **2015**, 6, 7903.
- [33] W. Rehman, R. L. Milot, G. E. Eperon, C. Wehrenfennig, J. L. Boland, H. J. Snaith, M. B. Johnston, L. M. Herz, *Adv. Mater.* **2015**, 27, 7938.
- [34] H. Sun, H. He, M. Yin, H. Cheng, X. Lin, Q. Huang, Y. Lu, *Opt. Mater. Express* **2021**, 11, 1874.
- [35] W. Rehman, R. L. Milot, G. E. Eperon, C. Wehrenfennig, J. L. Boland, H. J. Snaith, M. B. Johnston, L. M. Herz, *Adv. Mater.* **2015**, 27, 7938.
- [36] S. G. Motti, F. Krieg, A. J. Ramadan, J. B. Patel, H. J. Snaith, M. V. Kovalenko, M. B. Johnston, L. M. Herz, *Adv. Funct. Mater.* **2020**, 30, 1909904.
- [37] D. Zhao, H. Hu, R. Haselsberger, R. A. Marcus, M.-E. Michel-Beyerle, Y. M. Lam, J.-X. Zhu, C. La-O-Vorakiat, M. C. Beard, E. E. M. Chia, *ACS Nano* **2019**, 13, 8826.
- [38] J. Lloyd-Hughes, T.-I. Jeon, *J. Infrared Millim Terahertz Waves* **2012**, 33, 871.
- [39] N. Smith, *Phys. Rev. B* **2001**, 64, 155106.
- [40] L. Protesescu, S. Yakunin, M. I. Bodnarchuk, F. Krieg, R. Caputo, C. H. Hendon, R. X. Yang, A. Walsh, M. V. Kovalenko, *Nano Lett.* **2015**, 15, 3692.
- [41] K. Galkowski, A. Mitoglu, A. Miyata, P. Plochocka, O. Portugall, G. E. Eperon, J. T.-W. Wang, T. Stergiopoulos, S. D. Stranks, H. J. Snaith, R. J. Nicholas, *Energy Environ. Sci.* **2016**, 9, 962.
- [42] P. Papagiorgis, L. Protesescu, M. V. Kovalenko, A. Othonos, G. Itkos, *J. Phys. Chem. C* **2017**, 121, 12434.
- [43] P. Papagiorgis, A. Manoli, S. Michael, C. Bernasconi, M. I. Bodnarchuk, M. V. Kovalenko, A. Othonos, G. Itkos, *ACS Nano* **2019**, 13, 5799.
- [44] I. M. Eich, H. Beisinghoff, R. M. Knodler Ohl, M. Sprave, J. Vydra, M. Eckl, M. Dorr, R. Zentel, M. Ahlheim, M. Stahelin, B. J. Zysset, L. R. L. J. Zyss, B. C. J. Mello, H. Felix Wittmann, *Adv. Mater.* **1997**, 9, 230.
- [45] J. R. Lakowicz, *Principles of Fluorescence Spectroscopy*, Springer, Berlin **2006**.
- [46] R. Ulbricht, E. Hendry, J. Shan, T. F. Heinz, M. Bonn, *Rev. Mod. Phys.* **2011**, 83, 543.